

Kinematics Characteristic Analysis of an Airborne SAR Stabilized Platform Based on Finite-Step-Integration Method

1st Bo Han

School of Mechanical Engineering
Yanshan University
Qinhuangdao, China
bohan@ysu.edu.cn

2nd Shaozhe Li

School of Mechanical Engineering
Yanshan University
Qinhuangdao, China
lishaozhe202202@163.com

3rd Yuan Jiang✉

School of Mechanical Engineering
Yanshan University
Qinhuangdao, China
shadovor@foxmail.com

4th Jinming Dong

School of Mechanical Engineering
Yanshan University
Qinhuangdao, China
jmdong0823@163.com

5th Yuanzhi Zhou

School of Mechanical Engineering
Yanshan University
Qinhuangdao, China
yzzhou28@foxmail.com

6th Yongsheng Zhao

School of Mechanical Engineering
Yanshan University
Qinhuangdao, China
yszhao@ysu.edu.cn

Abstract—The high-quality operation of an airborne SAR system depends on the stable posture of the photoelectric system. For the requirement, this paper proposes an airborne SAR stabilized platform with omnidirectional posture adjustment capability based on a cubic 3-RRS parallel manipulator (PM). The kinematics characteristics of the airborne stabilized platform (ASP) are analyzed comprehensively based on Finite-Step-Integration (FSI) method. The ASP's forward kinematics position solution, accessible workspace, and singular boundary are obtained via analyzing, and the motion trajectory characteristics (angular velocity and acceleration) are analyzed based on the free control of the FSI method to the actuators' functions. The airborne SAR stabilized platform shows good performances on various kinematics characteristics, and provides a theoretical design and analysis guidance for the research of similar auxiliary equipment.

Keywords—airborne stabilized platform, cubic parallel manipulator, FSI method, kinematics characteristic

I. INTRODUCTION

Airborne Synthetic Aperture Radar (SAR) has the capability of all-weather, all-day, and long-distance imaging. It also possesses penetration capabilities for certain obstacles, allowing the acquisition of target information from multiple directions [1]-[3]. As a result, it has found extensive applications in both national economy and defense construction. However, the quality of SAR imaging can be significantly affected when there are changes in aircraft attitude or other disturbances, leading to insufficient image clarity [4], [5]. The role of an airborne SAR stabilizing platform is to serve as a motion compensation execution mechanism, isolating body disturbances and stabilizing the antenna beam direction [6]-[8]. Therefore, to maintain the imaging quality of airborne SAR, the design and development of airborne stabilizing platforms are also continuously underway.

Traditional airborne SAR stabilizing platforms are generally based on gimbal structures, employing electromechanical two-axis (azimuth and elevation) or three-axis (azimuth, elevation, and roll) multi-frame structures [9]-[11]. However, with the development of radar phased array technology, multi-frame structures struggle to achieve multi-dimensional antenna beam stability and demand increasingly

complex mechanisms for higher precision. To overcome the limitations of multi-frame structures, a three-axis cantilevered airborne stabilizer platform has been designed, which offers a larger range of motion and enhances the imaging quality of airborne cameras [12],[13]. Nevertheless, this type of stabilizing platform still faces challenges in practical applications, such as load-bearing capacity, disturbance resistance, kinematic characteristics, and strict limitations on weight and volume. Furthermore, a novel airborne stabilizer platform is proposed, which employs magnetic servo technology and integrates a control system into a universal joint structure. This integrated platform aims to offer enhanced stabilization and precise control for various airborne applications [14],[15]. However, magnetic drive technology remains a developing field, and its manufacturing costs are not yet cost-effective.

To address the aforementioned challenges, this paper proposes an Airborne Stabilized Platform (ASP) with omnidirectional attitude adjustment capabilities, based on a cube-like 3-RRS parallel manipulator. This stabilizing platform possesses the advantages of compact structure, high load capacity, flexibility, and stability. Additionally, using the Finite-Step-Integration (FSI) method, this paper conducts a comprehensive analysis of the kinematic characteristics of the ASP, providing theoretical design and analytical guidance for similar auxiliary devices.

II. AIRBORNE SAR STABILIZED PLATFORM AND THE FSI METHOD

A. Configuration Analysis

In this paper, a parallel stabilizing platform for airborne SAR based on the cube-like 3-RRS mechanism is designed. The degrees of freedom of this mechanism are analyzed using screw theory. The schematic diagram of the mechanism's kinematics is illustrated in Fig. 1.

When the mechanism is in its initial position, the second-level revolute joints of the three motion branches are located within the orthogonal frames of the rack $\mathcal{F}: \{x, y, z, \mathbf{O}\}$ in the xOy , yOz , and zOx planes, respectively. Additionally, the first-stage linkages are mutually perpendicular to the two links of the second stage. The axes of rotation of the first-level revolute joints in this cubic angle platform mechanism are

* Corresponding Author: Yuan Jiang; e-mail: shadovor@foxmail.com

mutually perpendicular, and evenly distributed, and all the links are of equal length.

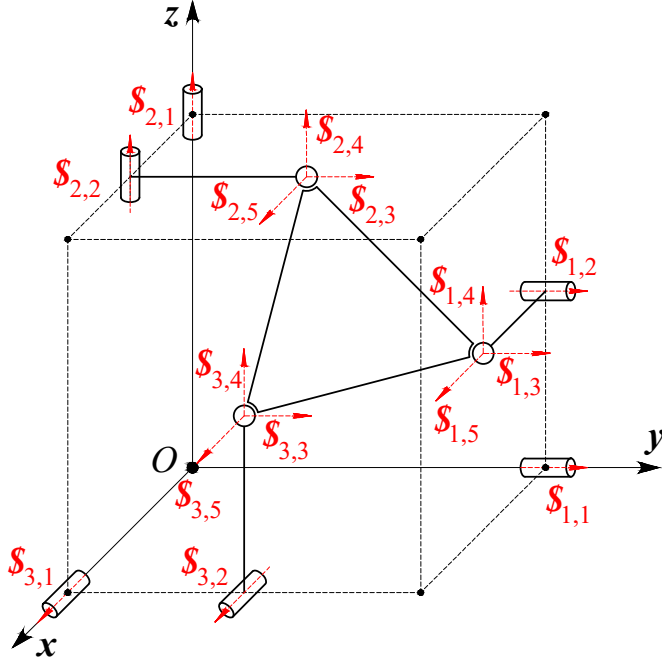


Fig. 1. Kinematics diagram of ASP mechanism

Based on the above information, the kinematic screw system for one of the motion branches of the cubic 3-RRS motion is determined as follows:

$$\begin{cases} \mathcal{S}_{1,1} = (0 \ 1 \ 0 \ ; \ 0 \ 0 \ 0)^T \\ \mathcal{S}_{1,2} = (0 \ 1 \ 0 \ ; \ -f_1 \ 0 \ d_1)^T \\ \mathcal{S}_{1,3} = (0 \ 1 \ 0 \ ; \ -f_2 \ 0 \ d_2)^T \\ \mathcal{S}_{1,4} = (0 \ 0 \ 1 \ ; \ M \ -d_2 \ 0)^T \\ \mathcal{S}_{1,5} = (1 \ 0 \ 0 \ ; \ 0 \ f_2 \ -M)^T \end{cases} \quad (1)$$

Hence, the constrained screw system for one of the motion branches of the cubic 3-RRS mechanism is as follows:

$$\mathcal{S}_{0,1}^r = (0 \ 1 \ 0 \ ; \ -f_2 \ 0 \ d_2)^T \quad (2)$$

By extension, the constraint screw system for the entire mechanism can be expressed as follows:

$$\begin{cases} \mathcal{S}_1^r = (0 \ 1 \ 0 \ ; \ -f_2 \ 0 \ d_2)^T \\ \mathcal{S}_2^r = (0 \ 0 \ 1 \ ; \ e_3 \ -d_5 \ 0)^T \\ \mathcal{S}_3^r = (1 \ 0 \ 0 \ ; \ 0 \ f_6 \ -e_6)^T \end{cases} \quad (3)$$

From the constrained screw system, it can be observed that the three constrained screw axes intersect at a single point in space and are linearly independent, thus restricting the mobile platform's movement in all directions.

To sum up, each motion branch allows the mobile platform to rotate in any direction while imposing force constraints on the platform's movement in all directions. As a result, the cubic 3-RRS mechanism can be classified as a parallel structure with three degrees of freedom.

B. The FSI method

Given that the position and orientation of the mobile platform in three-dimensional space can be uniquely determined by three non-collinear points on the platform, the fundamental principle of the FSI method is to segment the motion of a parallel mechanism into a finite number of segments. This approach transforms the static solution of forward kinematic analysis into a dynamic linear superposition process. The process of forward kinematic analysis using the FSI method is depicted in Fig. 2.

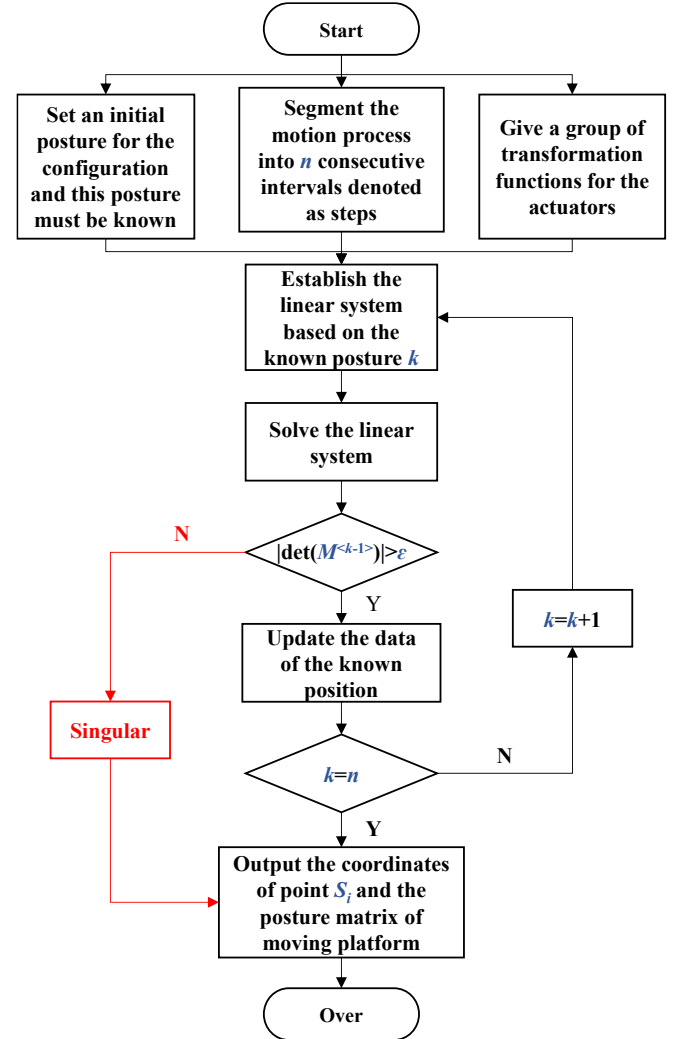


Fig. 2. Operation process of the FSI method.

Information regarding the driving joints is known, and the complete range of motion for the driving joints is divided into n finite intervals. Through the establishment and solution of linear equation systems, the positional information of the motion platform at the end of the k -th small interval can be derived. This obtained positional data is then utilized as known values for the subsequent iteration rounds, which are carried out a finite number of times. The outcome achieved at the completion of the final iteration (i.e., when $k=n$) represents the desired target position of the motion platform under the specified driving conditions. Within the algorithmic process, a series of coefficient matrices M are involved, with the coefficient matrix at the conclusion of the $(k-1)$ -th small interval denoted as $M^{<k-1>}$. The parameter ϵ functions as a threshold to determine the mechanism's singular configuration

at each step. If the determinant of the coefficient matrix surpasses the value of parameter ε , it indicates that the mechanism is in a singular position.

III. KINEMATICS CHARACTERISTICS ANALYSIS

A. Forward kinematics

The ASP proposed in this paper, as depicted in Fig. 3, is a three-degree-of-freedom airborne SAR parallel stabilizing platform based on the cubic 3-RRS architecture. It enables three-axis rotation in space. The first-level revolute joint is composed of a servo motor, turntable, linkage, and a bracket (fixed to the frame). The second-level revolute joint is constructed using pins, linkages, and related standard components. The ball joint is affixed to the motion platform and is constrained to follow the platform's three-dimensional rotations in space. The servo motor drives the motion of the first-level revolute joint, which is then transmitted through the second-level revolute joint, ultimately conveying the motion to the motion platform, enabling a responsive motion of the platform to the input.

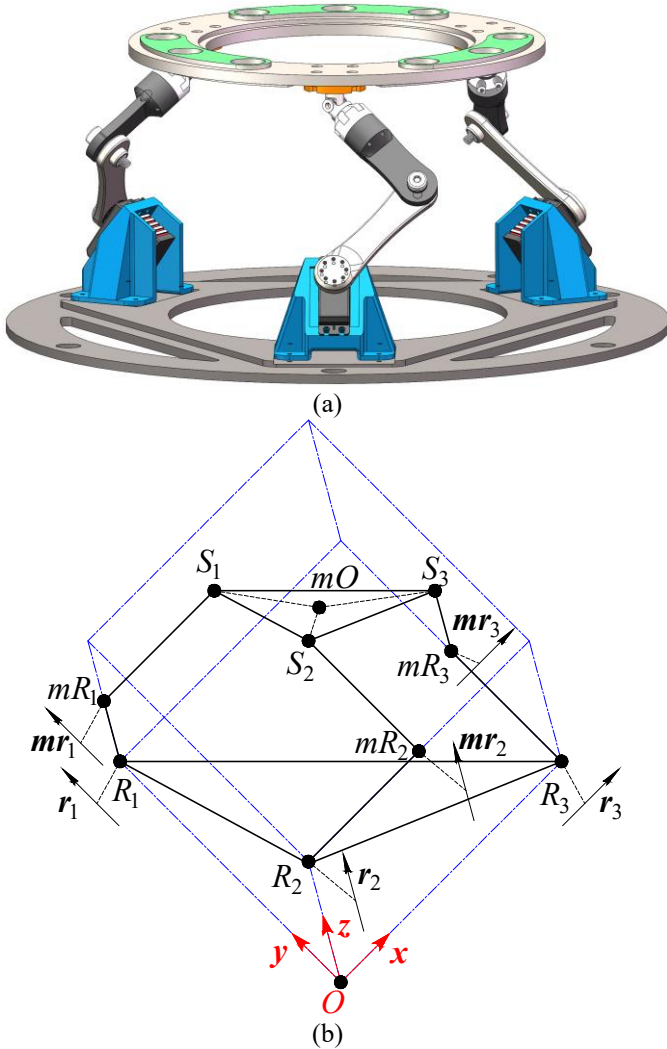


Fig. 3. The airborne stabilized platform: (a) The components of the ASP and (b) its intrinsic configuration.

For the sake of analysis, the center point (centroid) of each motion joint is selected as the reference point. Among them, point mO represents the center point of the moving platform. Furthermore, the initial pose information of the ASP is considered a known condition. During the motion of the

mechanism, when the driving joints rotate by a certain angle θ , the motion platform reaches the target pose. The FSI method divides the motion process into a set of n finite intervals.

The initial pose coordinates of the motion joints in the ASP are designated as $S_i^{(0)}, mR_i^{(0)}$, and $R_i^{(0)}$ ($i=1,2,3$), respectively, where the index " i " denotes the i -th motion branch. Additionally, each incremental rotational interval in the motion sequence is predetermined as a known value of θ_i/n degrees.

The process of establishing the first category of motion equations, as depicted in Fig. 4, derives from the fact that within the mechanism's motion, the second rotational joint mR_i , undergoes rotation solely around the first rotational joint R_i . Similarly, the spherical joint S_i , rotates exclusively about the second rotational joint mR_i . Consequently, the dynamic progression of the controlled motion branch can be described as follows:

In the first phase, an initial rotation is imparted to the first rotational joint R_i . This rotation subsequently induces a certain angular displacement in the second rotational joint mR_i , and the spherical joint S_i , while preserving their relative positions.

In the second phase, the spherical joint S_i , rotates around the second rotational joint mR_i , by an angle $\alpha_i^{<k>}$, thereby attaining the target pose. Given that the entire motion sequence is partitioned into a finite number of infinitesimal stages ($n \rightarrow \infty$), the value of the angle $\alpha_i^{<k>}$ is exceedingly small. By leveraging differential principles to effect linearization, within the isosceles triangle $\Delta mR_i^{(k)} S_i^{(k)} S_i^{(k)}$, it follows that $\lim_{n \rightarrow \infty} \angle mR_i^{(k)} S_i^{(k)} S_i^{(k)} = \lim_{n \rightarrow \infty} \angle mR_i^{(k)} S_i^{(k)} S_i' = 90^\circ$ ($k=1 \dots n$).

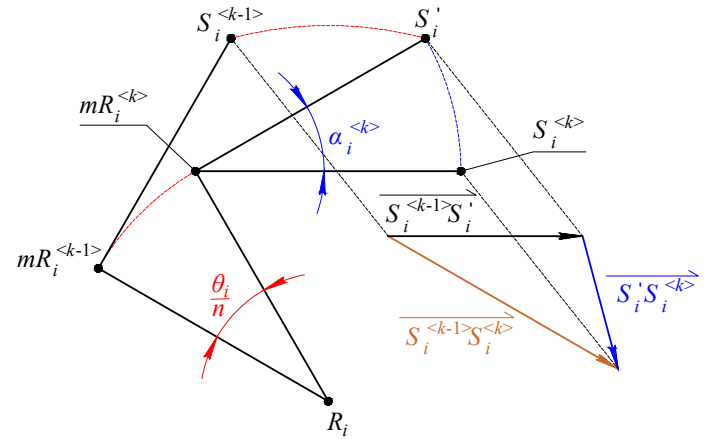


Fig. 4. Geometric principle of the first-type equations

$$\begin{cases} \overline{mR_i^{(k)} S_i'} \cdot \overline{S_i' S_i^{(k)}} = 0 \\ \overline{S_i^{(k-l)} S_i^{(k)}} = \overline{S_i' S_i^{(k)}} + \overline{S_i' S_i^{(k)}} \end{cases} \quad (4)$$

Upon simplification, the resultant form is as follows:

$$\overline{mR_i^{(k)} S_i'} \cdot \left(\overline{S_i^{(k-l)} S_i^{(k)}} - \overline{S_i^{(k-l)} S_i'} \right) = 0 \quad (5)$$

Within the aforementioned equation, vectors $\overline{mR_i^{(k)}S_i'}$ and $\overline{S_i^{(k-1)}S_i'}$ can be derived through the process of rotating vector $\overline{mR_i^{(k-1)}S_i^{(k-1)}}$ around R_i by an angle of θ_i/n .

The derivation process for the second category of motion equations is illustrated in Fig. 5. Considering that the motion platform exhibits displacement during its rotational movement, the motion of the platform within each infinitesimal interval can be conceptually divided into a preliminary translation along vector $\overline{mO^{(k-1)}mO^{(k)}}$, followed by a subsequent rotation of an angle $\beta_i^{<k>}$ about point $mO^{(k)}$. Under the premise of a sufficiently large n , the angle $\beta_i^{<k>}$ becomes exceptionally minute within each minuscule interval. Through the application of differential principles to attain linearity, within the confines of the isosceles triangle $\Delta mO^{(k)}S_i^{(k)}S_i^{(k-1)}$, it can be deduced

$$\lim_{n \rightarrow \infty} \angle mO^{(k)}S_i^{(k)}S_i^{(k-1)} = \lim_{n \rightarrow \infty} \angle mO^{(k)}S_i^{(k)}S_i' = 90^\circ (k = 1 \cdots n).$$

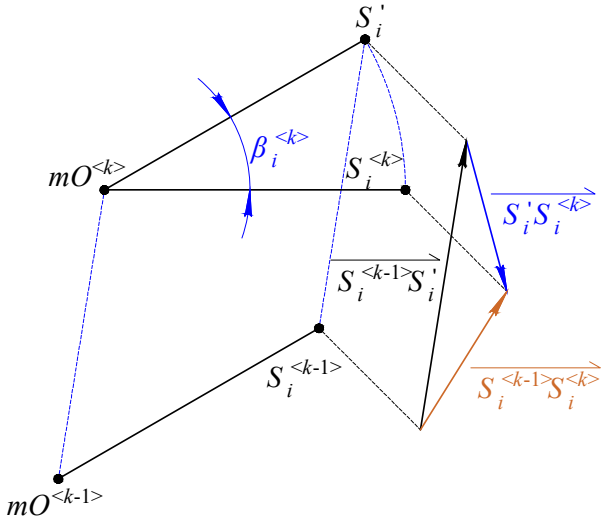


Fig. 5. Geometric principle of the second-type equations

$$\begin{cases} \overline{mO^{(k)}S_i'} \cdot \overline{S_i'S_i^{(k)}} = 0 \\ \overline{S_i'S_i^{(k)}} = \overline{S_i^{(k-1)}S_i'} - \overline{S_i^{(k-1)}S_i^{(k)}} \\ \overline{mO^{(k-1)}mO^{(k)}} = \overline{S_i^{(k-1)}S_i'} \\ \overline{mO^{(k-1)}S_i^{(k-1)}} = \overline{mO^{(k)}S_i'} \end{cases} \quad (6)$$

Upon simplification, the resultant form is as follows:

$$\overline{mO^{(k-1)}S_i^{(k-1)}} \cdot (\overline{mO^{(k-1)}mO^{(k)}} - \overline{S_i^{(k-1)}S_i^{(k)}}) = 0 \quad (7)$$

The third category of motion equations: When analyzed within the coordinate system of the motion platform, it is deduced from the configuration characteristics of the ASP that throughout the motion process, the three spherical joints remain consistently within a single plane. Additionally, their relative positions remain constant. The spherical joints along the three motion branches are uniformly distributed along a circle with the motion platform's center as its origin.

$$\overline{mO^{(k)}S_i^{(k)}} + \overline{mO^{(k)}S_2^{(k)}} + \overline{mO^{(k)}S_3^{(k)}} = 0 \quad (8)$$

The establishment process of the fourth category of motion equations is illustrated in Fig. 6. In light of the intrinsic characteristics of the ASP mechanism, it is evident that throughout the motion sequence, the spherical joints along the motion branches consistently lie within planes perpendicular to the axes of their respective first-level rotational joints.

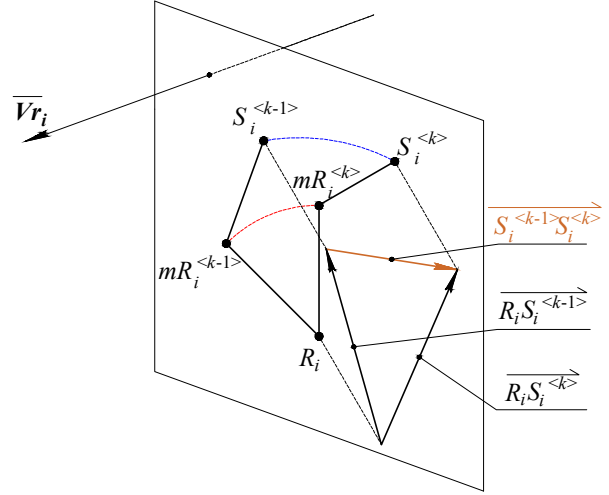


Fig. 6. Geometric principle of the fourth-type equations

$$\begin{cases} \overline{Vr_i} \cdot \overline{R_iS_i^{(k-1)}} = \overline{Vr_i} \cdot \overline{R_iS_i^{(k)}} \\ \overline{S_i^{(k-1)}S_i^{(k)}} = \overline{R_iS_i^{(k)}} - \overline{R_iS_i^{(k-1)}} \end{cases} \quad (9)$$

Thus, it follows:

$$\overline{Vr_i} \cdot \overline{S_i^{(k-1)}S_i^{(k)}} = 0 \quad (10)$$

By combining equations (5), (7), (8), and (10), a system of 12 linear equations can be constructed, yielding 12 unknown variables. The coefficient matrix of this linear system is denoted as $M_{12 \times 12}$. The matrix of unknown variables for the constraint system is $d_{12 \times 1}$, and the constant vector matrix of the constraint system is $c_{12 \times 1}$.

Consequently, the systematic formulation of constraint equations can be succinctly articulated as:

$$M_{12 \times 12} \cdot d_{12 \times 1} = c_{12 \times 1} \quad (11)$$

The solution to the 12 unknown variables in the matrix $d_{12 \times 1}$ can be deduced from the above equation. By implementing MATLAB to compile a forward kinematic analysis program and iteratively solving it n times, the attitude of the ASP's rotational platform end can be determined.

To validate the reliability of the FSI method for obtaining solutions in forward kinematic analysis, an ASP mechanism model was established in the ADAMS software (as shown in Fig. 7), and subjected to simulation analysis. Three distinct driving input functions were employed: $15\sin(2\pi/5 \cdot t)$, $10\sin(\pi/5 \cdot t)$, and $-10\sin(2\pi/5 \cdot t)$. The simulation duration was set to 10 seconds, with the motion process segmented into n intervals, where n equaled 15000. In order

to ascertain the spatial position and orientation of the ASP system, the centers of the spherical joints connected to the three motion branches were selected as observation points. The trajectories of the observation points' coordinates over time were compared with the results obtained from the FSI method (including true and computed values). The simulation comparison outcomes are depicted in Fig. 8.

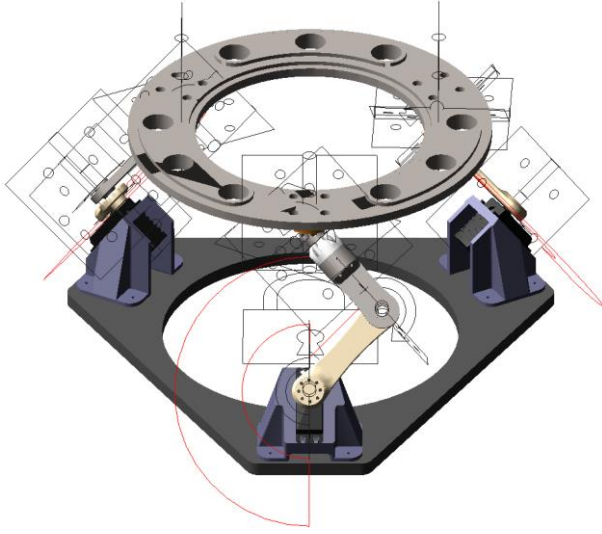


Fig. 7. ASP mechanism simulation model

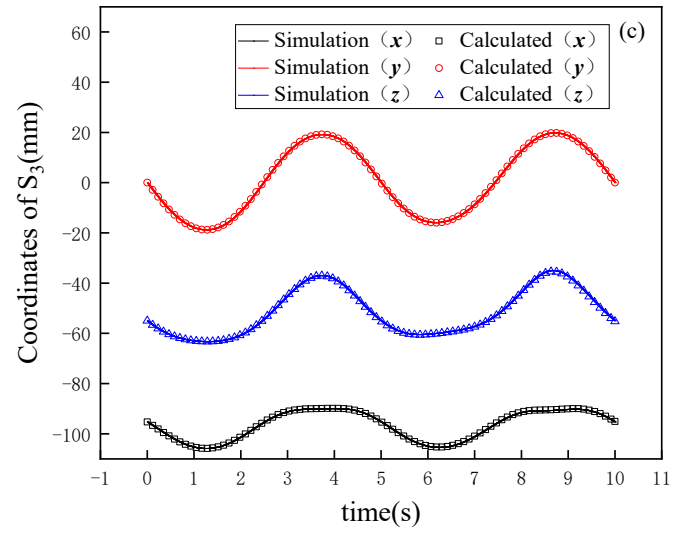
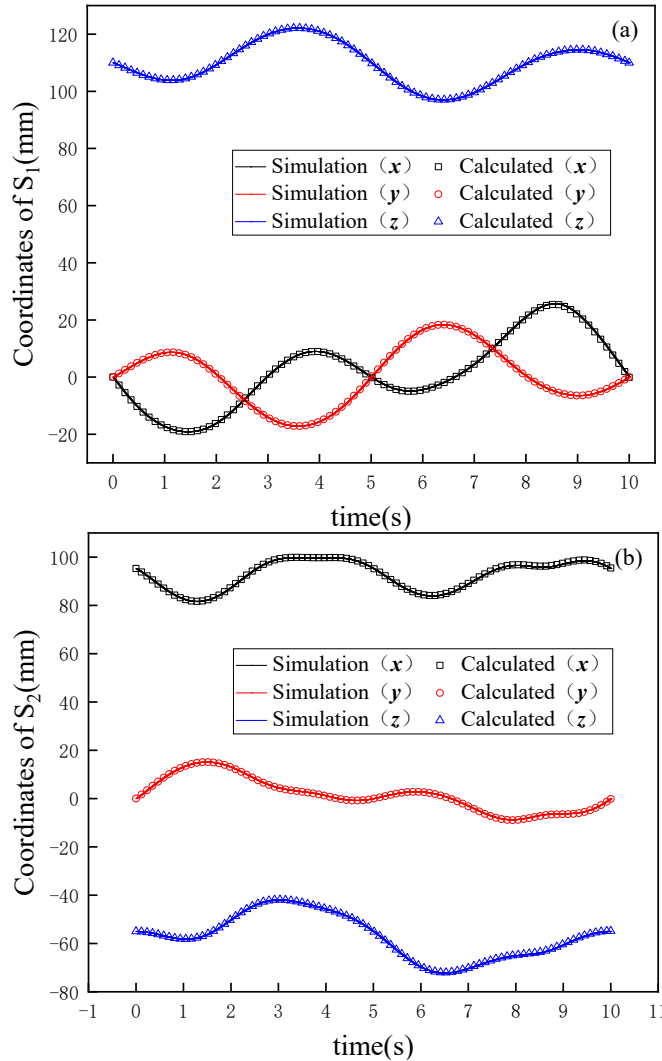
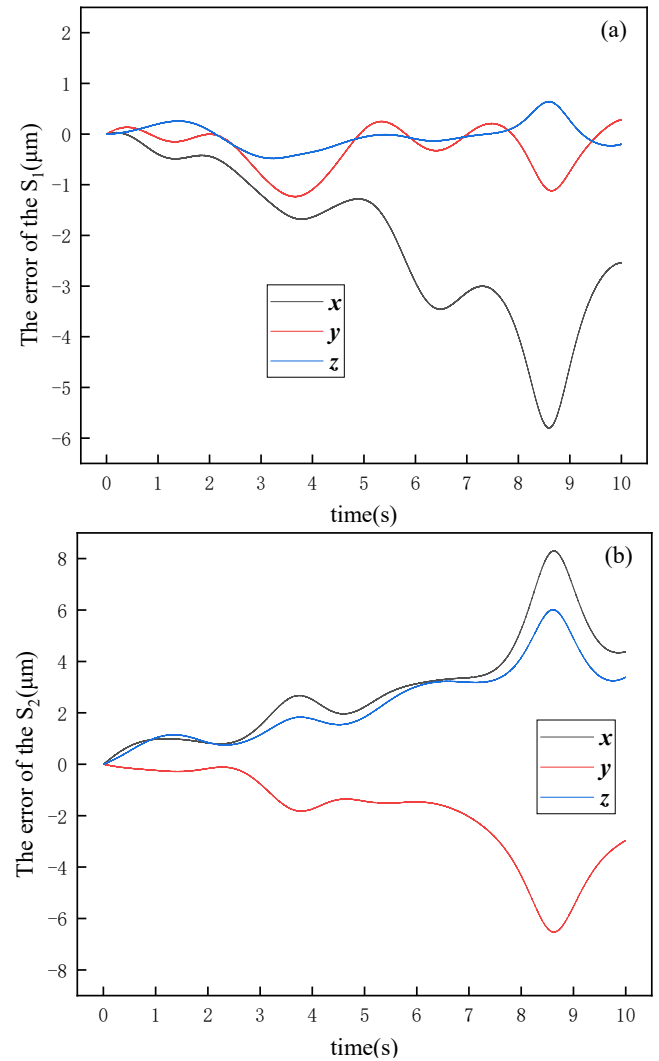


Fig. 8. The reference point movement trajectory. (a), (b), and (c) respectively represent in each case the change of the coordinate values of the reference points on the branch chain 1, 2, and 3 with the time under the influence of the driving joint.

As deduced from the above, the error between computed values and actual values can be calculated and is depicted in Fig. 9.



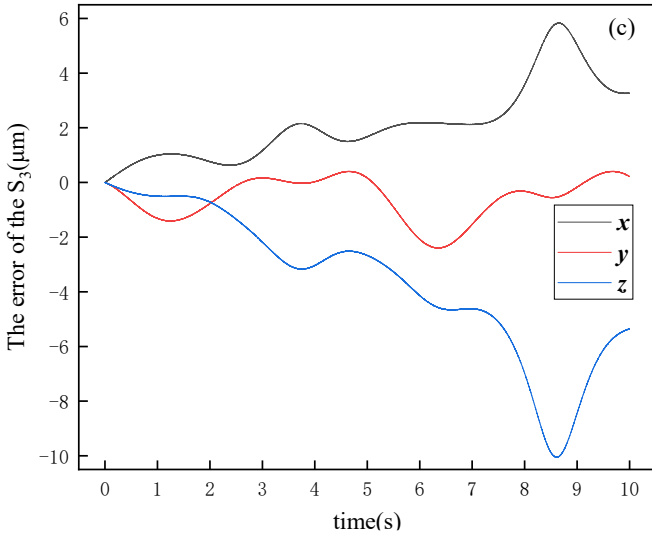


Fig. 9. (a), (b), and (c) represent the error between the calculated value and the true value of the reference point on the three driving branches respectively.

The analysis of the figure above demonstrates that the coordinates of the drive joints on the ASP platform vary over time, the coordinates of each drive joint were computed using the FSI method. By comparing and analyzing the computed values of the drive joint coordinates in three drive branches (obtained through the FSI method) with the real values (obtained through simulation), the results of this analysis indicate that the error between the results obtained using the FSI method and the real values is minimal, approximately around 20 micrometers.

This suggests that the analysis conducted using the FSI method closely aligns with the real-world scenario, with very small discrepancies in the computed values. This underscores the reliability of the FSI method for kinematic analysis. Furthermore, the FSI method proves to be a trustworthy analytical approach suitable for the study of the ASP platform or similar mechanical systems. This holds significance for the field of engineering and other domains where modeling and analysis of complex systems are essential.

B. Motion trajectory characteristics

The determination of motion trajectory characteristics using the FSI method involves conducting finite-order differentiations for each driving function within every motion interval " T/n ". This process results in obtaining the variations in each small motion interval " $\Delta\theta_k/n$ ". Essentially, we calculate the rate of change for each driving function, effectively dividing the entire motion time T into n small intervals.

Subsequently, we employ the FSI kinematic forward solution model to calculate the coordinates of spatial points at discrete time instances. This allows us to determine the positions of spatial points at different time points. By calculating the difference between the coordinates of a point at a specific time and those at the preceding time, we obtain the displacement " ΔS ", representing the distance the object has moved within this small time interval. Dividing " ΔS " by the time interval " Δt " yields the average velocity " v ", which represents the average speed of the reference point during this small time span.

Similarly, by subtracting the average velocity of the preceding time span from that of the given interval, we can ascertain the velocity difference " Δv ", indicating the change in velocity. Dividing " Δv " by " Δt " allows for the derivation of the average acceleration during that specific interval.

This approach enables us to calculate and analyze the motion trajectory characteristics of any mechanical structure's reference point under the influence of different driving functions. A higher order of differentiation for the driving functions, corresponding to smaller motion intervals " T/n ," yields more precise motion trajectory characteristics.

In this study, we focus specifically on the velocity and acceleration profiles of the origin of the moving platform. We utilize three representative driving functions: $15\sin(2\pi/5 \cdot t)$, $10\sin(\pi/5 \cdot t)$, and $-10\sin(2\pi/5 \cdot t)$. Utilizing the FSI method, we calculate and simulate the motion trajectory characteristics. We efficiently derive the velocity and acceleration profiles of the moving platform's origin using MATLAB code compilation, as visually presented in Figure 10(a). Furthermore, we evaluate the accuracy of our simulations by comparing the velocity and acceleration errors between the calculated values and the true values, as illustrated in Figure 10(b). These analyses enhance our understanding of the motion characteristics and performance of objects during different time intervals.

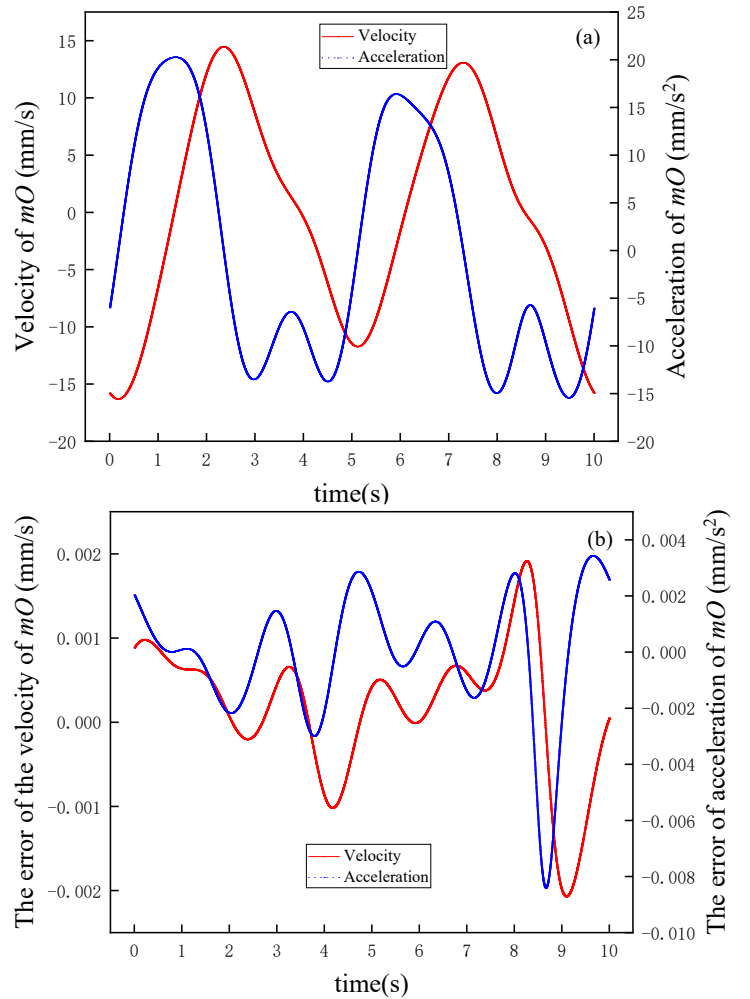


Fig. 10. Velocity and acceleration analysis of the origin of the moving platform: (a) Velocity and acceleration curves; (b) The error curve of velocity and acceleration

Based on the analysis results from Figure 10(a), the ASP platform exhibits remarkable performance in terms of its velocity and acceleration characteristics when influenced by the three representative driving functions. Furthermore, an examination of Figure 10(b) reveals that, through a comparative analysis of velocity errors between calculated and actual values, the velocity error remains within 4 micrometers per second, and the acceleration error remains within 14 micrometers per second. This underscores the precision of employing the FSI method for assessing the motion characteristics of the ASP platform.

IV. CONCLUSION

In conclusion, this study presents a novel SAP and investigates its kinematic characteristics. The FSI method for solving the forward kinematics of parallel mechanisms is introduced. Using the FSI method with given input functions for the driving joints, the position solution of the ASP is obtained, and simulation verification is performed in ADAMS. The results demonstrate that the ASP exhibits excellent performance in various motion characteristics, and the FSI method efficiently and accurately establishes and solves the forward kinematic characteristics of parallel mechanisms. In summary, the proposed ASP in this paper offers theoretical design and analytical guidance for similar auxiliary devices' research.

ACKNOWLEDGMENT

This research was supported by the National Natural Science Foundation of China (Grant No. 52105035), the Natural Science Foundation of Hebei Province of China (Grant No. E2021203109), the Science and Technology Research Project of Hebei Province of China (Grant No. 236Z1801G), and the Industrial Robot Control and Reliability Technology Innovation Center of Hebei Province (Grant No. JXKF2105).

REFERENCES

- [1] A. Moreira, P. Prats-Iraola, M. Younis, G. Krieger, I. Hajnsek, and K. P. Papathanassiou, "A tutorial on synthetic aperture radar," *IEEE Geoscience and Remote Sensing Magazine*, vol. 1, no. 1, pp. 6-43, 2013.
- [2] A. C. Mondini, F. Guzzetti, K.-T. Chang, O. Monserrat, T. R. Martha, and A. Manconi, "Landslide failures detection and mapping using Synthetic Aperture Radar: Past, present and future," *Earth-Science Reviews*, vol. 216, 2021.
- [3] K. Ouchi, "Recent Trend and Advance of Synthetic Aperture Radar with Selected Topics," *Remote Sensing*, vol. 5, no. 2, pp. 716-807, 2013.
- [4] J. Chen, M. Xing, H. Yu, B. Liang, J. Peng, and G.-C. Sun, "Motion Compensation/Autofocus in Airborne Synthetic Aperture Radar: A Review," *IEEE Geoscience and Remote Sensing Magazine*, vol. 10, no. 1, pp. 185-206, 2022.
- [5] J. Li, Y. Wang, Z. Lu, and Y. Li, "Instantaneous observable degree modeling based on movement measurement for airborne POS," *Aerospace Science and Technology*, vol. 84, pp. 916-925, 2019.
- [6] J. M. Hilkert, "Inertially stabilized platform technology Concepts and principles," *IEEE Control Systems*, vol. 28, no. 1, pp. 26-46, 2008.
- [7] M. K. Masten, "Inertially stabilized platforms for optical imaging systems," *IEEE Control Systems*, vol. 28, no. 1, pp. 47-64, 2008.
- [8] J. Xiu, P. Huang, J. Li, H. Zhang, and Y. Li, "Line of Sight and Image Motion Compensation for Step and Stare Imaging System," *Applied Sciences*, vol. 10, no. 20, 2020.
- [9] Z. Hurak and M. Rezac, "Image-Based Pointing and Tracking for Inertially Stabilized Airborne Camera Platform," *IEEE Transactions on Control Systems Technology*, vol. 20, no. 5, pp. 1146-1159, 2012.
- [10] X. Zhou, G. Gong, J. Li, H. Zhang, and R. Yu, "Decoupling control for a three-axis inertially stabilized platform used for aerial remote sensing," *Transactions of the Institute of Measurement and Control*, vol. 37, no. 9, pp. 1135-1145, 2014.
- [11] D. Mei and Z.-Q. Yu, "Disturbance rejection control of airborne radar stabilized platform based on active disturbance rejection control inverse estimation algorithm," *Assembly Automation*, vol. 41, no. 5, pp. 525-535, 2021.
- [12] A. Altan and R. Hacıoğlu, "Model predictive control of three-axis gimbal system mounted on UAV for real-time target tracking under external disturbances," *Mechanical Systems and Signal Processing*, vol. 138, 2020.
- [13] Y. Yang, C. Yu, Y. Wang, N. Hua, and H. Kuang, "Imaging Attitude Control and Image Motion Compensation Residual Analysis Based on a Three-Axis Inertially Stabilized Platform," *Applied Sciences*, vol. 11, no. 13, 2021.
- [14] L. Zhuchong, L. Kun, and Z. Wei, "Inertially Stabilized Platform for Airborne Remote Sensing Using Magnetic Bearings," *IEEE/ASME Transactions on Mechatronics*, vol. 21, no. 1, pp. 288-301, 2016.
- [15] T. Wen and B. Xiang, "The airborne inertially stabilized platform suspend by an axial-radial integrated active magnetic actuator system," *J Adv Res*, vol. 31, pp. 191-205, Jul 2021.